The Astrophysical Journal, 810:142 (13pp), 2015 September 10 doi:10.1088/0004-637X/810/2/142

TIME DEPENDENCE OF THE e^- FLUX MEASURED BY *PAMELA* DURING THE 2006 JULY–2009 DECEMBER SOLAR MINIMUM

O. Adriani[1,2], G. C. Barbarino[3,4], G. A. Bazilevskaya[5], R. Bellotti[6,7], M. Boezio[8], E. A. Bogomolov[9], M. Bongi[1,2], V. Bonvicini[8], S. Bottai[2], A. Bruno[6,7], F. Cafagna[7], D. Campana[4], P. Carlson[10], M. Casolino[11], G. Castellini[12], C. De Donato[13], C. De Santis[11], N. De Simone[13], V. Di Felice[13,14], V. Formato[8,15], A. M. Galper[16], A. V. Karelin[16], S. V. Koldashov[16], S. Koldobskiy[16], S. Y. Krutkov[9], A. N. Kvashnin[5], A. Leonov[16], V. Malakhov[16], L. Marcelli[11], M. Martucci[11,17], A. G. Mayorov[16], W. Menn[18], M. Mergè[11,13], V. V. Mikhailov[16], E. Mocchiutti[8], A. Monaco[6,7], N. Mori[2], R. Munini[8,19], G. Osteria[4], F. Palma[11,13], B. Panico[4], P. Papini[2], M. Pearce[10], P. Picozza[11,13], M. Ricci[17], S. B. Ricciarini[12], R. Sarkar[8,20], V. Scotti[3,4], M. Simon[18], R. Sparvoli[11,13], P. Spillantini[1,2], Y. I. Stozhkov[5], A. Vacchi[8,21], E. Vannuccini[2], G. Vasilyev[9], S. A. Voronov[16], Y. T. Yurkin[16], G. Zampa[8], N. Zampa[8], M. S. Potgieter[22], and E. E. Vos[22]
[1] University of Florence, Department of Physics, I-50019 Sesto Fiorentino, Florence, Italy
[2] INFN, Sezione di Florence, I-50019 Sesto Fiorentino, Florence, Italy
[3] University of Naples "Federico II," Department of Physics, I-80126 Naples, Italy
[4] INFN, Sezione di Naples, I-80126 Naples, Italy
[5] Lebedev Physical Institute, RU-119991, Moscow, Russia
[6] University of Bari, Department of Physics, I-70126 Bari, Italy
[7] INFN, Sezione di Bari, I-70126 Bari, Italy
[8] INFN, Sezione di Trieste, I-34149 Trieste, Italy
[9] Ioffe Physical Technical Institute, RU-194021 St. Petersburg, Russia
[10] KTH, Department of Physics, and the Oskar Klein Centre for Cosmoparticle Physics, AlbaNova University Centre, SE-10691 Stockholm, Sweden
[11] University of Rome "Tor Vergata," Department of Physics, I-00133 Rome, Italy
[12] IFAC, I-50019 Sesto Fiorentino, Florence, Italy
[13] INFN, Sezione di Rome "Tor Vergata," I-00133 Rome, Italy
[14] Agenzia Spaziale Italiana (ASI) Science Data Center, Via del Politecnico snc, I-00133 Rome, Italy
[15] INFN, Sezione di Perugia, I-06123 Perugia, Italy
[16] National Research Nuclear University MEPhI, RU-115409 Moscow, Russia
[17] INFN, Laboratori Nazionali di Frascati, Via Enrico Fermi 40, I-00044 Frascati, Italy
[18] Universität Siegen, Department of Physics, D-57068 Siegen, Germany
[19] University of Trieste, Department of Physics, I-34147 Trieste, Italy
[20] Indian Centre for Space Physics, 43 Chalantika, Garia Station Road, Kolkata 700084, West Bengal, India
[21] University of Udine, Department of Mathematics and Informatics, I-33100 Udine, Italy
[22] Centre for Space Research, North-West University, 2520 Potchefstroom, South Africa
Received 2015 June 18; accepted 2015 August 1; published 2015 September 8

ABSTRACT

Precision measurements of the electron component of cosmic radiation provide important information about the origin and propagation of cosmic rays in the Galaxy not accessible from the study of cosmic-ray nuclear components due to their differing diffusion and energy-loss processes. However, when measured near Earth, the effects of propagation and modulation of Galactic cosmic rays in the heliosphere, particularly significant for energies up to at least 30 GeV, must be properly taken into account. In this paper the electron (e^-) spectra measured by the *Payload for Antimatter Matter Exploration and Light-nuclei Astrophysics* down to 70 MeV from 2006 July to 2009 December over six-month time intervals are presented. Fluxes are compared with a state-of-the-art three-dimensional model of solar modulation that reproduces the observations remarkably well.

Key words: cosmic rays – solar wind – Sun: heliosphere

1. INTRODUCTION

Electrons are the most abundant negatively charged component of cosmic rays but constitute only about 1% of the total cosmic-ray flux. Precise measurements of the energy spectrum of cosmic-ray electrons provide important information for the understanding of the origin and propagation of cosmic rays in the Galaxy that is not accessible from the study of the cosmic-ray nuclear components. Because of their low mass, electrons undergo severe energy loss through synchrotron radiation in the magnetic field and inverse Compton scattering with the ambient photons.

There are two prominent origins of high-energy electrons in the cosmic radiation: primary electrons accelerated at sources such as supernova remnants, e.g., Allen et al. (1997), Aharonian et al. (2004), and secondary electrons produced by processes such as nuclear interactions of cosmic rays with the interstellar matter. Additional sources of electrons such as pulsars, e.g., Atoyan et al. (1995), or dark matter particles, e.g., Cirelli et al. (2008), cannot be excluded. Both these additional sources were invoked to explain the measured positron fraction (Adriani et al. 2009a; Ackermann et al. 2012; Aguilar et al. 2013). The study of precise measurements of the energy spectrum of cosmic-ray electrons can shed light on their origin and propagation through the galaxy, e.g., Delahaye et al. (2010), Bisschoff & Potgieter (2014). However, the majority of the measurements and the totality of those for energies greater than 100 MeV were obtained with experiments in the proximity of the Earth, well inside the heliosphere. Therefore, the effects of the solar wind and heliospheric magnetic field (HMF) cannot be neglected. As cosmic rays traverse the turbulent magnetic field embedded in the solar wind, particles are scattered by its irregularities and undergo convection, diffusion, and adiabatic

deceleration in the expanding solar wind. Gradient, curvature, and current sheet drifts also have an effect that is dominant during periods of minimum solar activity, e.g., see the overview by Potgieter (2013). Cosmic rays with rigidities up to tens of GV are affected but the largest effect is seen at low rigidities (less than a few GV), e.g., Strauss & Potgieter (2014a).

In 2012 August, *Voyager 1* crossed the heliopause, widely considered to be the modulation boundary, and is now inside the very local interstellar medium (Gurnett et al. 2013). For the first time, the very local interstellar spectra (LIS) at low energies, including the electron LIS between 5 and 20 MeV, have been observed, e.g., Stone et al. (2013), Webber et al. (2013), and Potgieter (2014a). Together with the *Payload for Antimatter Matter Exploration and Light-nuclei Astrophysics* (*PAMELA*) measurements at higher energies, these observations make it possible to properly address a major uncertainty in what the total modulation of these cosmic rays is between the modulation boundary and the Earth.

Furthermore, drift models predict a clear charge-sign dependence for the modulation of cosmic rays (Potgieter 2014b) whose effects are expected to be particularly evident at energies below a few GeV. During so-called $A < 0$ polarity cycles like solar cycle 23, when the HMF is directed toward the Sun in the northern hemisphere, negatively charged particles drift inward primarily through the polar regions of the heliosphere. Conversely, positively charged particles drift inward primarily through the equatorial regions of the heliosphere, encountering the wavy heliospheric current sheet in the process. The situation reverses when the solar magnetic field changes its polarity at each solar maximum, causing a clear 22 year cycle in the modulation of cosmic rays in the process.

The most recent period of solar minimum activity and the consequent minimum modulation conditions for cosmic rays were unusual. It was expected that the new activity cycle would begin early in 2008. Instead solar minimum modulation conditions continued until the end of 2009 when the largest fluxes of Galactic cosmic rays since the beginning of the space age were recorded (Mewaldt 2010; Potgieter et al. 2013a; Strauss & Potgieter 2014b). This period of prolonged solar minimum activity is well suited to studying the modulation processes that affect the propagation of Galactic cosmic rays inside the heliosphere.

Here results on the long-term variation in the energy spectrum of Galactic cosmic-ray electrons (e^-) measured down to 70 MeV are presented. These results are based on the data set collected by the *PAMELA* satellite-borne experiment (Picozza et al. 2007) between 2006 July and 2009 December. *PAMELA* is an instrument designed for cosmic-ray antimatter studies and has been flying on board the Russian *Resurs-DK1* satellite since 2006 June in a semi-polar near-Earth orbit. Results on the effects of the solar modulation on the energy spectra of Galactic cosmic-ray protons in the same period have already been published (Adriani et al. 2013a) with accompanying numerical modeling by Potgieter et al. (2014).

2. THE *PAMELA* INSTRUMENT

The *PAMELA* spectrometer (Picozza et al. 2007) was designed and built to study the antimatter component of cosmic rays from tens of MeV up to hundreds of GeV and with a significant increase in statistics with respect to previous experiments. To achieve this goal the apparatus was optimized

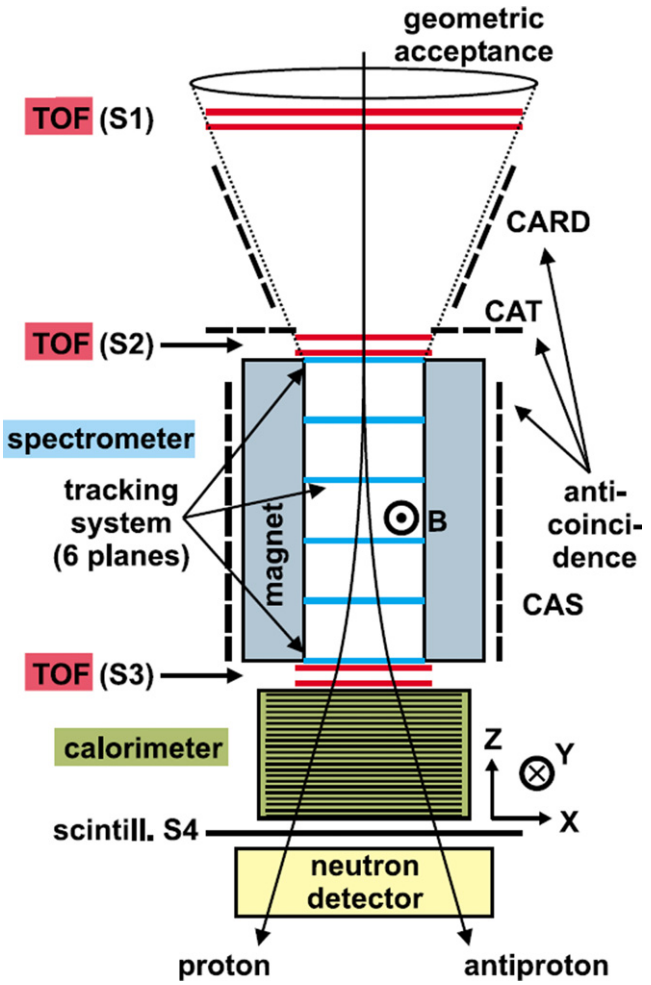

Figure 1. Schematic view of the *PAMELA* apparatus.

for the study of charge one particles and to reach a high level of electron–proton discrimination. The instrument, shown schematically in Figure 1, comprises the following subdetectors (from top to bottom): a time-of-flight system (ToF S1, S2, S3), a magnetic spectrometer, an anticoincidence system (CARD, CAT, CAS), an electromagnetic imaging calorimeter, a shower tail catcher scintillator (S4), and a neutron detector. These components are housed inside a pressurized container attached to the Russian *Resurs-DK1* satellite, which was launched on 2006 June 15. The orbital altitude varied between 350 and 600 km at an inclination of 70°.

The central components of *PAMELA* are a permanent magnet and a tracking system composed of six planes of double-sided silicon sensors, which form the magnetic spectrometer (Adriani et al. 2003). The main task of the magnetic spectrometer is to measure the particle rigidity $R = pc/\mathrm{Ze}$ (p and Ze being the particle momentum and charge, respectively, and c the speed of light) and the ionization energy losses (dE/dx). The rigidity measurement is done through the reconstruction of the trajectory based on the impact points on the tracking planes and the resulting determination of the curvature due to the Lorentz force. The ToF system (Osteria et al. 2004) comprises three double layers of plastic scintillator paddles with the first two (S1 and S2) placed above and the third (S3) immediately below the magnetic spectrometer, as shown in Figure 1. The ToF system provides measurements of

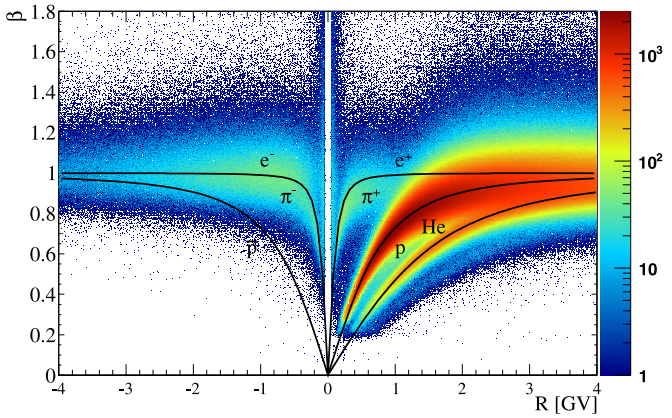

Figure 2. ToF velocity (β) as a function of the rigidity. The various particle species are indicated.

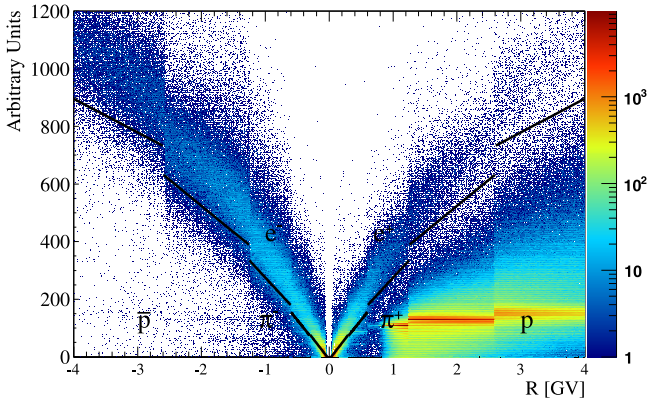

Figure 3. Quantity related to the topological development of the shower in the calorimeter as a function of rigidity for events selected with Criteria 1–7. The quantity computation uses the number of the plane closest to the shower maximum estimated for an electromagnetic shower of a given energy. The quantization of the plane numbers produce the shown discontinuities. The events above the solid lines are tagged as electrons by this selection.

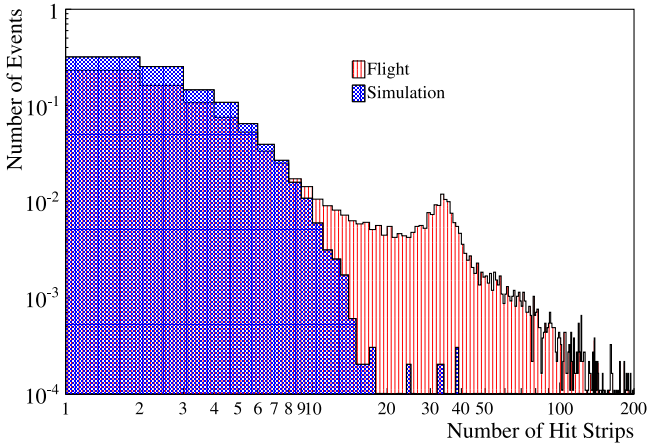

Figure 4. Normalized number of hit strips in the last 18 calorimeter planes for events selected with Criteria 1–7 and rigidity between 70 and 150 MV for experimental (red histogram) and simulated (blue histogram) data. The total number of events in both histograms is normalized to 1. The tail of the higher values in the number of hit strips for the experimental histogram is associated with a contamination of spillover protons traversing most of the calorimeter, with a peak around 35 due to non-interacting ones.

the particle velocity combining time of passage information with track length derived from the magnetic spectrometer. By measuring the particle velocity, direction, and curvature of the spectrometer, we can distinguish between down-going particles and up-going splash-albedo particles and separate negatively charged particles from positively charged particles.

The sampling imaging calorimeter (16.3 radiation lengths, 0.6 interaction lengths) is used for hadron–lepton separation, using topological and energetic information about the shower development in the calorimeter (Boezio et al. 2002). The shower tail catcher and the neutron detector (Stozhkov et al. 2005) beneath it provide additional information for the discrimination. An anticoincidence system is used to reject spurious events (Orsi et al. 2005).

The total weight of *PAMELA* is 470 kg while the power consumption is 355 W. A more detailed description of the instruments and the data handling can be found in Picozza et al. (2007).

3. DATA ANALYSIS

This work is based on data collected between 2006 July and 2009 December. The periods of time spent by the satellite in the South Atlantic Anomaly and during significant solar activity (i.e., 2006 December when a large solar event took place; Adriani et al. 2011a) were excluded from the data. Data are presented in six-month time periods, a compromise between statistically significant results and detailed analysis of the time variation of the fluxes.

3.1. Electron Selection

Clean events were selected requiring:

1. A single track fitted within the spectrometer fiducial volume where the reconstructed track is at least 1.5 mm away from the magnet walls.
2. Selected tracks must have at least three hits on the bending x-view, at least three hits on the non-bending y-view, and a track lever-arm of at least four silicon planes in the tracker.
3. A positive value for the velocity $\beta = v/c$ (v particle velocity, c speed of light) measured by the ToF system.

This set of basic criteria provided events with reliable measurements of the sign and absolute value of the particle rigidity and velocity. Figure 2 shows the distribution of the velocity (β) as a function of rigidity for these events. The spread in the values of β for relativistic particles is due to the finite time resolution of the ToF system. On the positive side the proton signal dominates, while on the negative side the electron signal clearly emerges as relativistic particles. However, additional particle species are present in the negatively charged sample. They are: antiprotons, pions and "spillover" protons. The Galactic antiproton component represents a contamination of a few percent over the entire rigidity range. The pion component is clearly visible below 300 MV in Figure 2 for both positive and negative rigidities. This component had already been studied for the antiproton analysis (Adriani et al. 2009b) using both simulated and flight data. The majority of these pion events had hits in the AC scintillators and/or large energy deposits in one of the top ToF scintillators clearly indicating that they were the product of cosmic-ray interactions with the *PAMELA* structure or pressure vessel. Spillover protons were mostly relativistic events with incorrect

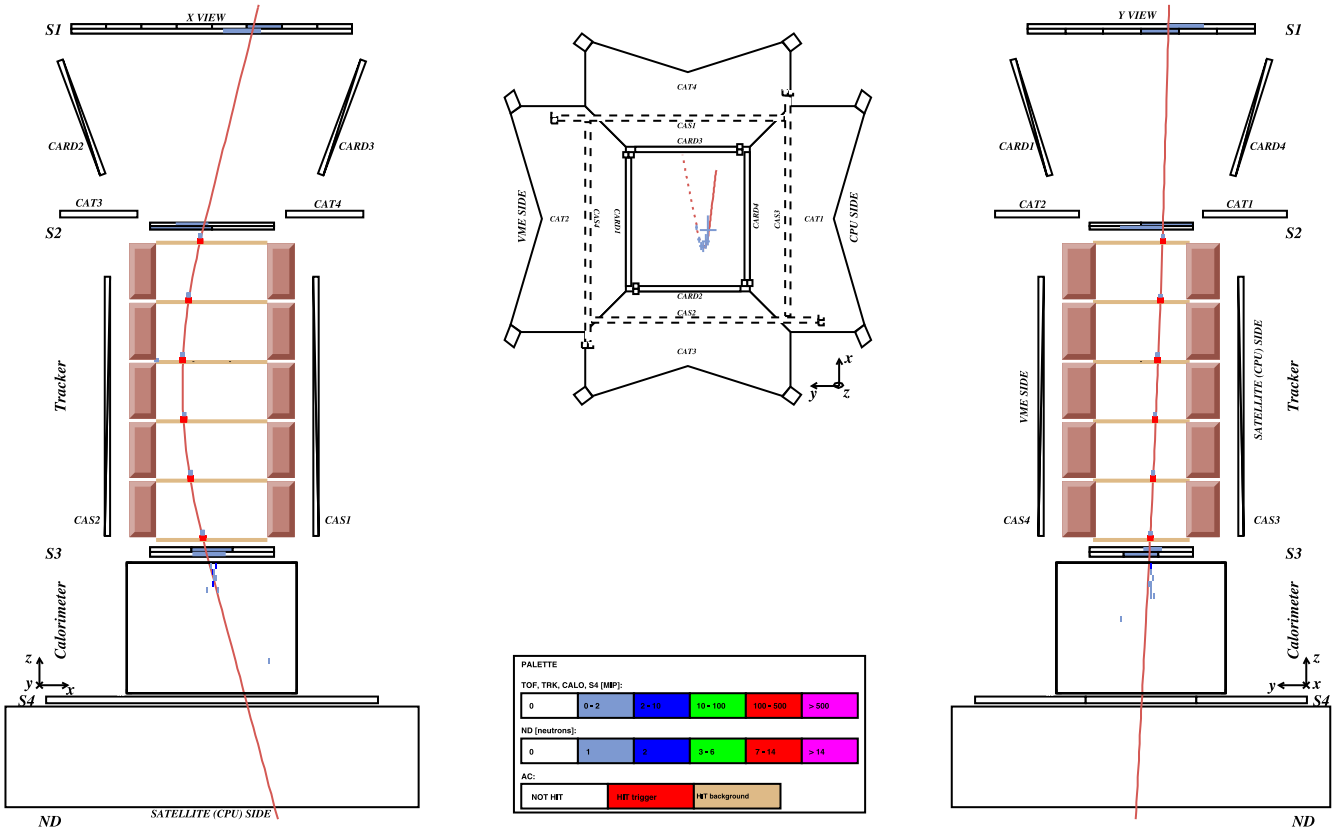

Figure 5. Event display of an electron event of ∼120 MV selected as having a low value in the experimental distribution of Figure 4. The bending (x) and non-bending (y) views are shown on the left and on the right, respectively. A plan view of *PAMELA* is shown in the center. The signal as detected by *PAMELA* detectors is shown along with the particle trajectory (red solid line) reconstructed by the fitting procedure of the tracking system.

determination of the charge sign. These events included: high-energy protons to which the wrong sign of the curvature was assigned due to the intrinsic deflection uncertainty in spectrometer measurements, protons that scattered in the material of the tracking system mimicking the trajectory of negatively charged particles and events with spurious hits in the tracker planes causing a wrong reconstruction of the curvature. The last two effects were the dominant causes for protons reconstructed with low negative rigidities. This contamination was particularly significant at very low rigidities (below ∼500 MV) where noisy strips could be taken as good points for the fit of a highly bent track when the minimum requirement on the number of hits on the x-view was just three, as in Criterion 2. For this reason, a more stringent criterion was used in place of Criterion 2 to evaluate the electron fluxes below 500 MV:

2bis: Selected tracks must have at least four hits on the bending x-view, at least three hits on the non-bending y-view, and a track lever-arm of at least four silicon planes in the tracker.

Then, additional selection criteria were introduced to select a sample of electrons that was as clean as possible:

4. No activity in the CARD and CAT scintillators of the anticoincidence system below 10 GV and no activity in the CAS scintillators below 300 MV.
5. Mean $dE/dx < 3$ mip (minimum ionizing particle units) in both ToF S1 and S2 scintillators.
6. Mean ionization energy losses (dE/dx) in the tracking system planes less than 1.8 mip.
7. Relativistic particles: $\beta > 0.9$.
8. Calorimeter selections.

Criteria 4–5 significantly reduced the pion contamination. The rigidity ranges for the anticounter selection were a compromise between residual pion contamination and electron selection efficiencies. As the electron energy rises, back-scattering from the electromagnetic shower in the calorimeter increases resulting in an increasing activity in the anti-coincidence scintillators. The different rigidity limit for CARD and CAT with respect to CAS was due to the different location of the scintillators with respect to the calorimeter (see Figure 1).

Criteria 6–7 were used to reduce the antiproton and pion contaminations to a negligible amount up to about 1.7 GV and about 250 MV, respectively. The residual pion and antiproton contaminations at higher rigidities and the spillover proton contamination were removed using the calorimeter information (Criterion 8).

The calorimeter selection was developed using a Monte Carlo simulation of the *PAMELA* apparatus based on the GEANT4 code (Agostinelli et al. 2003). The simulation reproduces the entire *PAMELA* apparatus, including the pressure vessel, and was validated using particle beam data. The longitudinal and transverse segmentation of the calorimeter allowed leptonic showers to be selected with high efficiency and small contamination above 300 MV. This information was used in previous analyses to successfully select positrons in a vast

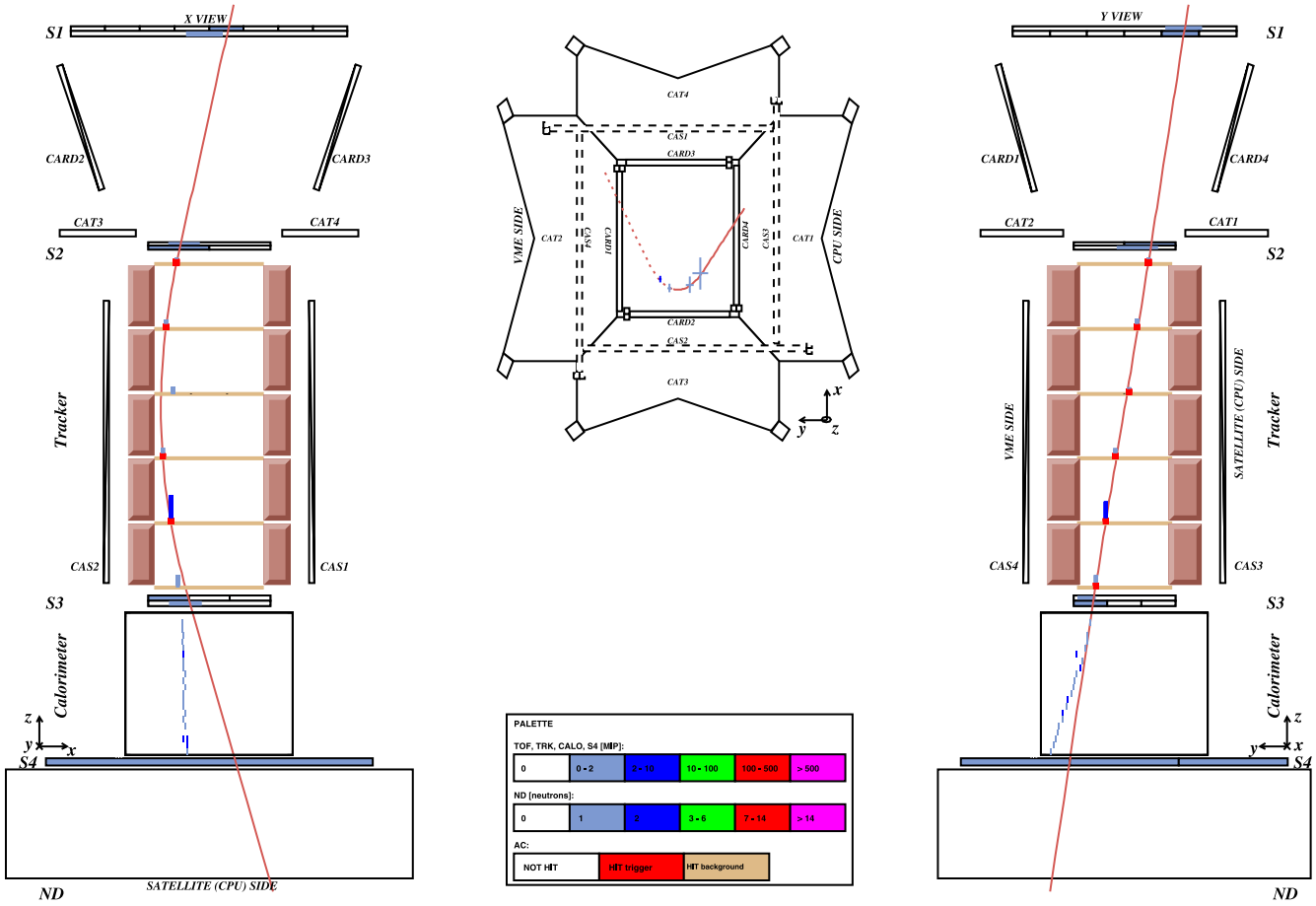

Figure 6. Event display of a spillover proton event of ∼110 MV selected from the peak around 35 in the experimental distribution of Figure 4. See Figure 5 for further details.

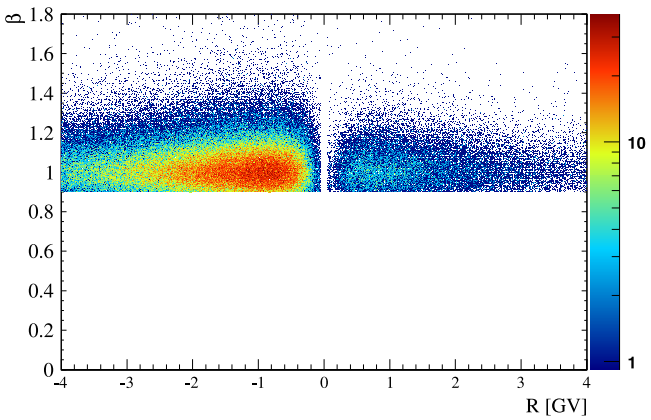

Figure 7. ToF velocity (β) as a function of rigidity for the events surviving all selection criteria including Criterion 7: $\beta > 0.9$.

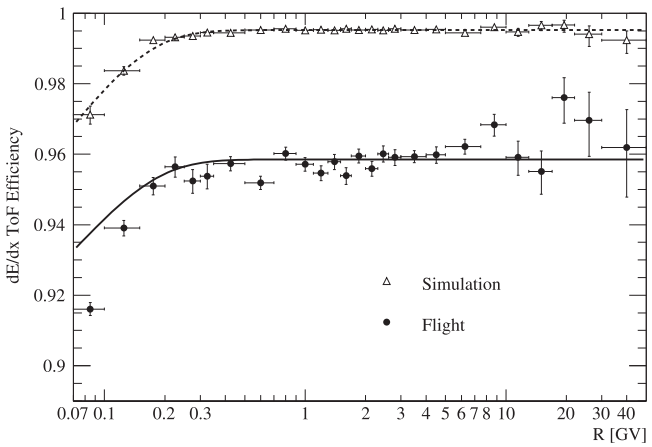

Figure 8. Efficiency of the ToF dE/dx selection (Criterion 5) as a function of rigidity for the first time interval (2006 July–November) for flight (full circles) and simulated (open triangles) data. The dashed line is a fit to the simulated data; the solid line is a fit to the experimental data based on the simulated shape and indicates the efficiency used in the data analysis.

background of protons (Adriani et al. 2009a, 2010, 2013b). The calorimeter electron selection was based on variables that emphasized the differences between the leptonic and hadronic showers such as multiplication with increasing calorimeter depth and the collimation of the electromagnetic cascade along the track. Figure 3 shows the distribution of one of these variables for the events surviving Criteria 1–7. This quantity, related to the multiplication of the leptonic shower, turned out to have large values for leptons and lower values for non-interacting and late interacting hadrons because of the limited number of secondaries in the hadronic shower. The solid lines in Figure 3 indicate the lower limit for electron selection based on this quantity. Combining several of these variables all residual contaminations were reduced to a negligible ($\ll$1%) amount from 350 MV up to the highest rigidities of this analysis (see also Munini 2012).

At the lowest rigidities (below 350 MV) spillover protons accounted for most of the residual contamination after selection

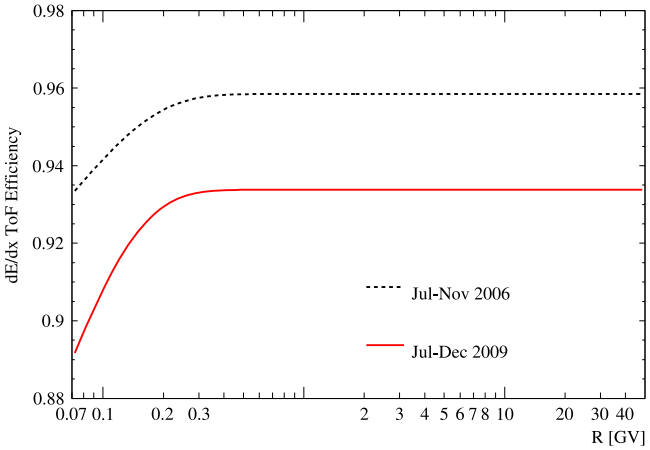

Figure 9. Temporal evolution of the ToF dE/dx selection efficiency. Black dashed line: efficiency for the first time interval (2006 July–November); red solid line: efficiency for the last time interval (2009 July–December).

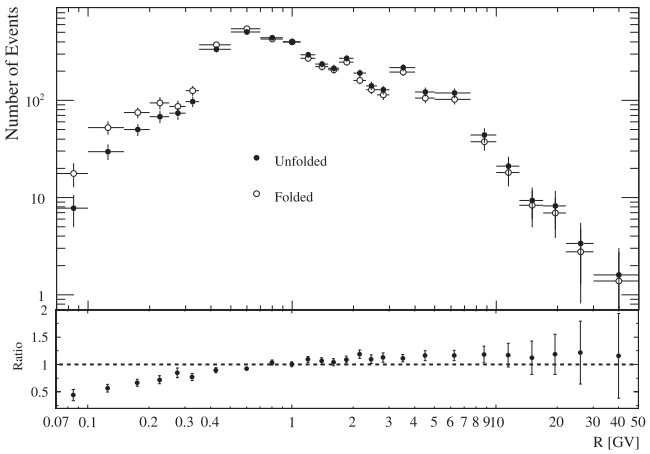

Figure 10. Top panel: distributions of the event counts, corrected for all selection efficiencies except those of selection Criteria 2 and 4, selected in the lowest geomagnetic cutoff interval (0–0.055 GV) before (open circles) and after (full circles) the unfolding procedure. Bottom panel: ratio between the unfolded and folded count distributions.

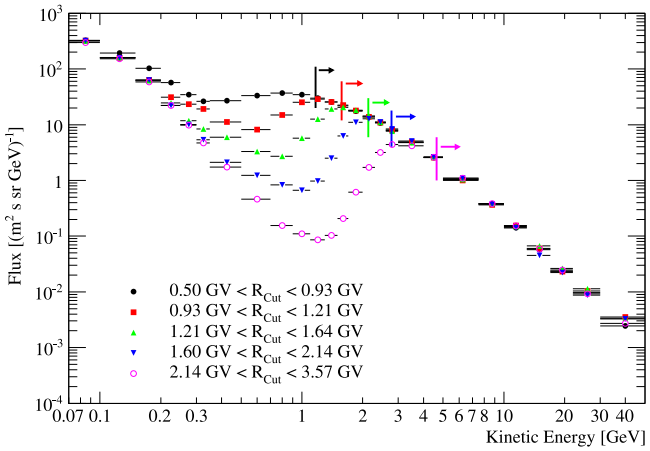

Figure 11. Electron (e^-) energy spectrum measured by *PAMELA* at the five geomagnetic rigidity cutoff ($R_{\rm Cut}$) intervals specified in the figure. The arrows indicate the energy regions where the Galactic electrons dominate and are unaffected by the Earth's magnetosphere. Around the geomagnetic cutoff, in the penumbral region, Galactic electrons are mixed with re-entrant albedo electrons that become the dominant component as the energies decrease.

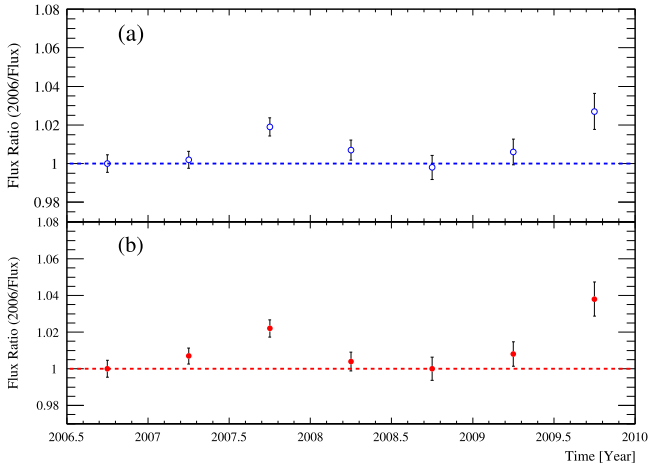

Figure 12. High-energy (30–50 GeV) proton flux measured in 2006 July–November divided by the proton fluxes measured in each time interval. Proton events were selected with the same requirements for electron analysis but with a calorimeter selection using Criterion 2bis (a) and Criterion 2 (b).

with Criteria 1–7 and were rejected using additional calorimeter variables that exploited the energy deposit in the bottom part of the calorimeter. Electromagnetic showers below about 0.5 GV mostly develop in the first half of the calorimeter, while spillover protons tend to traverse the entire volume. These features are illustrated in Figure 4 which shows the number of strips hit in the last 18 calorimeter planes for events selected with Criteria 1–7 and a rigidity between 70 and 150 MV from simulated (blue histogram) and experimental (red histogram) data. The tail of the higher values in the red histogram is associated with a contamination of high-energy particles traversing most of the calorimeter, with a peak around 35 due to non-interacting particles, while electron-like events account for the part of the distribution at low values as indicated by the consistency with the Monte Carlo data. This association is further confirmed by a visual inspection of events from the experimental distribution. Figures 5 and 6 show two typical events: one with a value of 2, consistent with an electron signal, and one with a value of 32, consistent with a contaminating spillover proton. A selection based on this and two related quantities rejected this type of contaminating event without significantly affecting the electron signal.

Figure 7 shows the distribution of the velocity as a function of rigidity for the events surviving all selection criteria. The residual contamination of pions, antiprotons, and spillover protons was assumed to be negligible over the entire rigidity range of interest for this work.

3.2. *Efficiency*

As can be seen in Figure 2, the majority of the negatively charged events were electrons. Along with the redundant information provided by the apparatus, this allowed the study of electron selection efficiencies to be conducted using flight data. Furthermore, the large collected statistics allowed the time dependence of the efficiencies to be monitored over a relatively short timescale. The efficiency study was complemented by an analysis of simulated data. With the Monte Carlo data it was possible to reproduce and study all selection efficiencies, their rigidity and time dependence also allowing the detection of possible sources of bias in the experimental evaluation of the efficiencies, like contamination of efficiency samples and

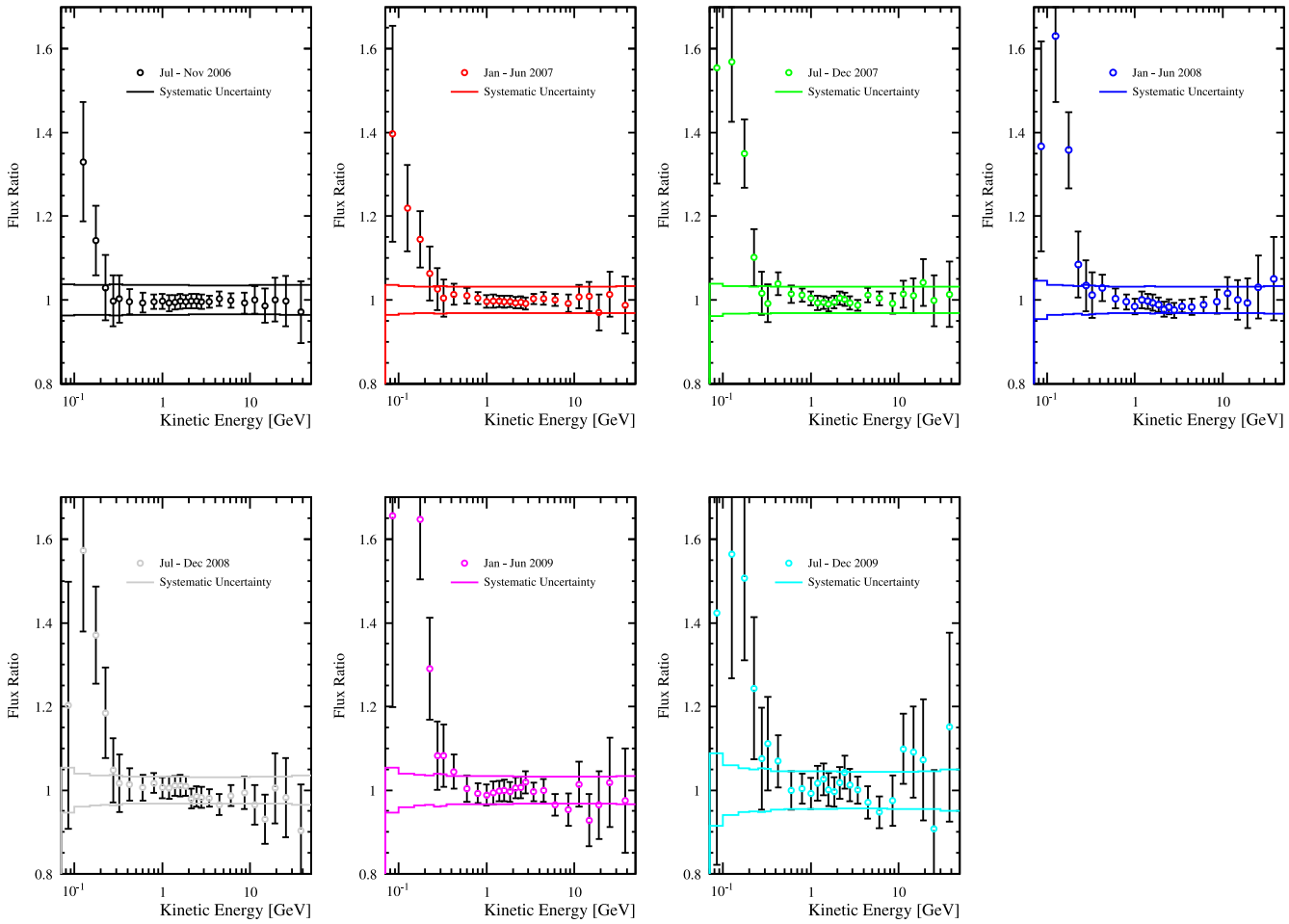

Figure 13. Electron fluxes measured in each time interval obtained with Criterion 2 divided by the equivalent ones obtained with Criterion 2bis. The solid lines indicate the systematic uncertainties associated with these data.

correlation among selection criteria. As an example, Figure 8 shows the efficiencies for the ToF dE/dx selection (Criterion 5) for the first time period (2006 July–November) as a function of rigidity. The efficiency sample, both experimental and simulated, was selected using all other selection criteria except for Criterion 5. Monte Carlo data showed that the ToF dE/dx selection efficiency was unaffected by the selections used to extract the efficiency sample. The full circles indicate the estimated experimental electron selection efficiency and the open triangles the simulated one. A slight difference ($\sim$3%) can be seen between the two sets of data, however, it should be noted that the shape of the flight data is well reproduced by simulations except at very low rigidities below about 150 MV. In this rigidity region the difference between experimental and simulated efficiencies increases to about 5% at 70 MV. This additional difference was due to a residual contamination in the experimental efficiency sample, as shown by a visual inspection of a random sample of events. In fact, it was noticed that only a combination of selections based on all *PAMELA* detectors was able to produce a clean electron sample at the lowest rigidities. Therefore, the ToF dE/dx selection efficiency was obtained fitting the flight data (solid line in Figure 8) with a functional shape based on the simulated data (dashed line in Figure 8). Figure 9 shows the resulting efficiency for Criterion 5 at the beginning and at the end of the data taking. A small time dependence (about 2% in nearly four years) of the efficiency can be noticed.

Similarly to the case of analysis of the proton flux (Adriani et al. 2011c, 2013a), the efficiency of the tracking system selection (Criteria 1 and 2), and especially its energy dependence, was obtained by Monte Carlo data. The tracking system selection efficiency was found to decrease over the years from a maximum of $\sim$90% in 2006 to $\sim$20% at the end of 2009 when Criterion 2 was used in the selection. With Criterion 2bis, the decrease in the efficiency was sharper, down to $\sim$10% at the end of 2009. This significant time dependence was due to the sudden, random failure of a few front-end chips in the tracking system. This resulted in a progressive reduction of the tracking efficiency, since the number of hits available for track reconstruction decreased. However, no degradation in the signal-to-noise ratio and spatial resolution was observed. The front-end chip failure was treated in the simulation with the inclusion of a time-dependent map of dead channels.

Another exception was the anticounter selection (Criterion 4) efficiency for which the simulated values were used. While there was an excellent agreement between the experimental and simulated efficiencies, the Monte Carlo predicted a dependence of the efficiency on the shape of the electron energy spectrum when measured as a function of rigidity in the spectrometer instead of energy at the top of the payload. Considering that the

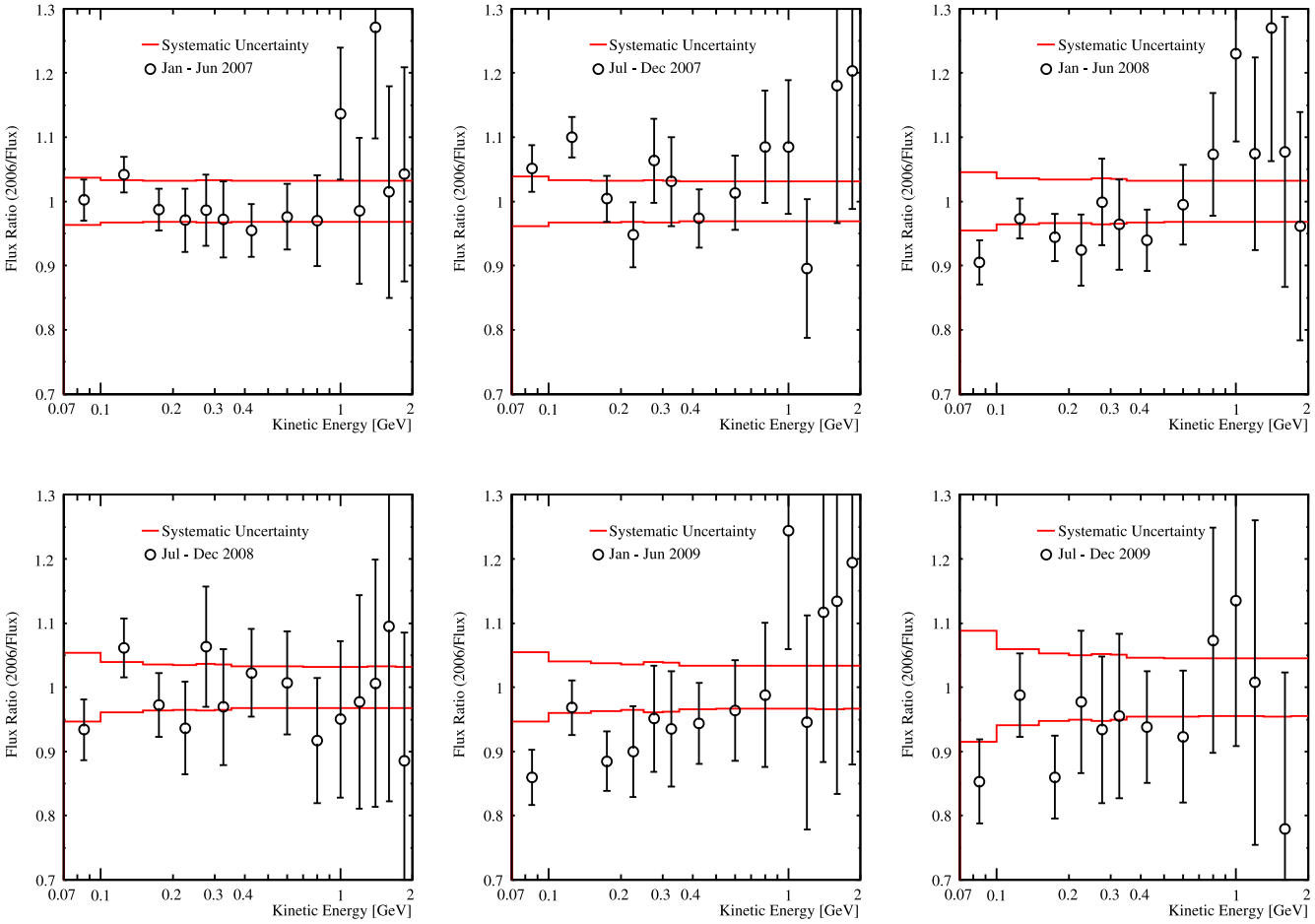

Figure 14. Re-entrant albedo e^- fluxes measured in 2006 July–November divided by the equivalent fluxes measured in the other time intervals. The solid lines indicate the systematic uncertainties associated with these data.

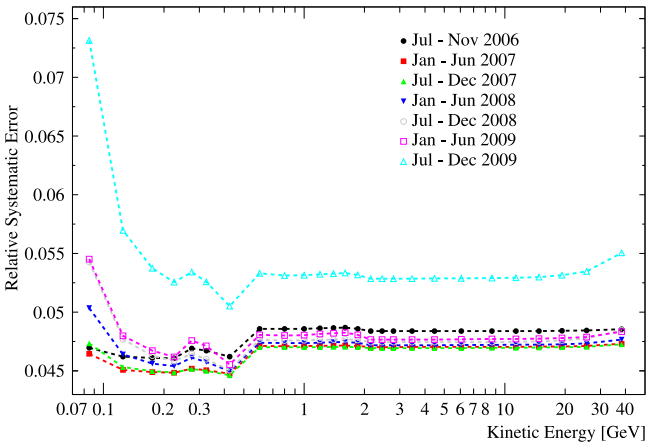

Figure 15. Relative systematic errors as a function of rigidity for the seven time intervals.

electron spectral shape varied significantly over the orbit due to the Earth's magnetic field (see Section 3.4), it was decided to correct the selected events distributed according to their energies reconstructed at the top of the payload, i.e., the unfolded count distribution, using the simulated efficiency; see the next section.

3.3. Spectral Unfolding

Since in this analysis the electron energies were obtained by measuring the deflections, hence the rigidities, of the particles in the magnet cavity, we had to properly account for both the response of the spectrometer and the energy losses suffered by the electrons prior to entering the tracking system. Particularly significant were energy losses due to bremsstrahlung of electrons while traversing the pressurized container and parts of the apparatus on top of the tracking system (equivalent to about 0.1 radiation lengths) since the resulting photons were able to traverse the spectrometer without being detected. Consequently the measured rigidities differed from the initial energies of the electrons at the top of the payload. To account for these effects a Bayesian unfolding procedure, as described in D'Agostini (1995), was applied to the count distributions of selected events binned according to their measured rigidities and divided by all selection efficiencies except those of the tracking system and anticounter selections. As discussed in the previous section, these were instead applied to the unfolded count distribution. Figure 10, top panel, shows the count distribution for the lowest geomagnetic cutoff interval (0–0.055 GV) before (open circles) and after (full circles) the unfolding procedure. The bottom panel shows the variation of counts in each rigidity (in the spectrometer)/energy (at the top of the payload) bin resulting from the unfolding procedure.

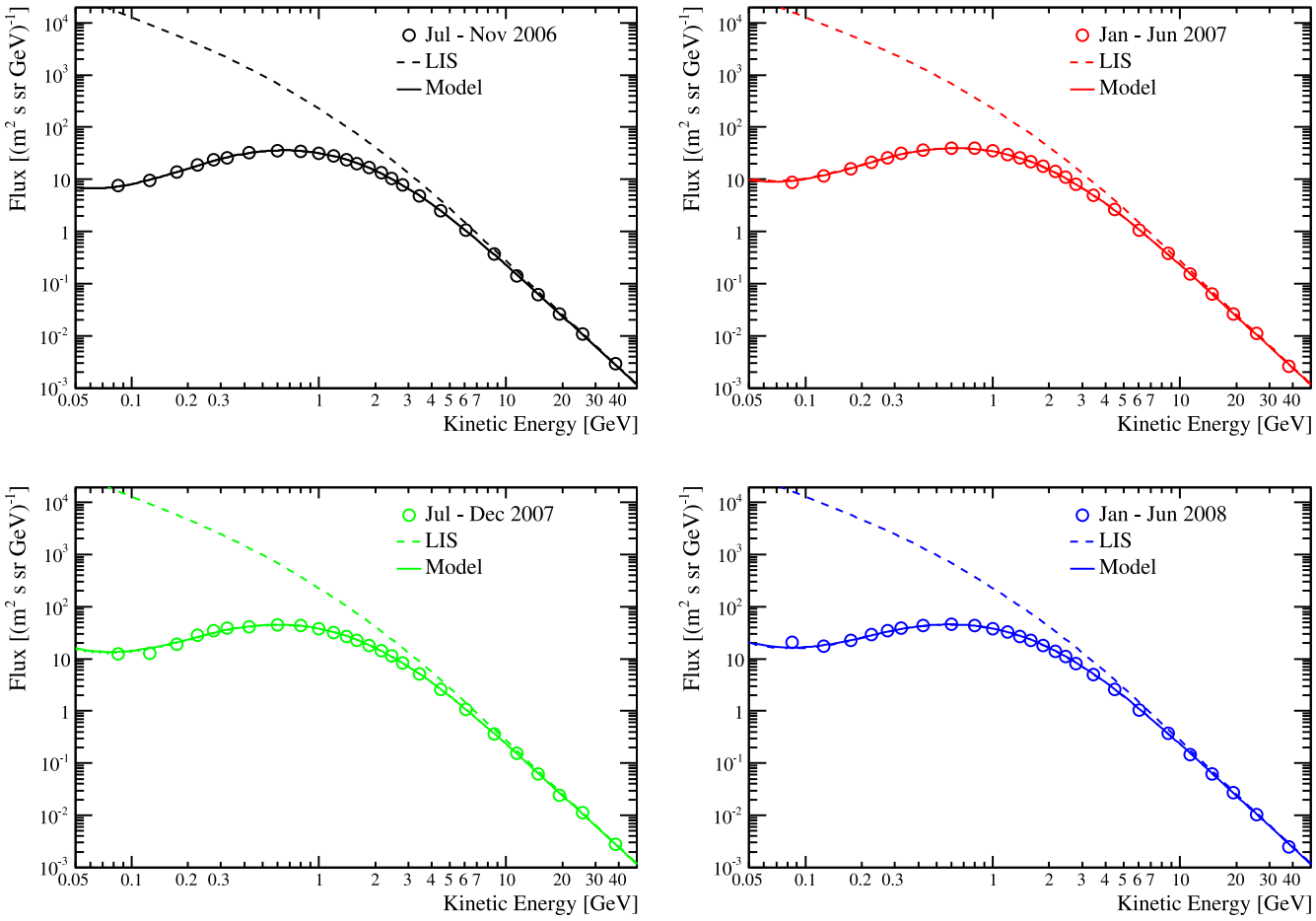

Figure 16. Measured electron (e^-) energy spectrum for the first half-year periods from the second half of 2006 to the first half of 2008. Time progresses from top to bottom and left to right. The error bars are the quadratic sum of the statistical and systematic errors. If not visible, they lie inside the data points. The computed spectra (solid lines) and the LIS used for the computation (dashed line) are also shown.

3.4. Flux Determination

The fluxes $\phi(E)$ (E kinetic energy) were evaluated as follows:

$$\phi(E) = \frac{N(E)}{\epsilon(E) \times G(E) \times T \times \Delta E} \quad (1)$$

where $N(E)$ is the unfolded count distribution, $\epsilon(E)$ is the efficiency of the remaining tracking system and anticounter selections, $G(E)$ is the geometrical factor, T is the live time, and ΔE is the width of the energy interval.

The geometrical factor, i.e., the requirement of triggering and containment, at least 1.5 mm away from the magnet walls and the TOF-scintillator edges, was estimated with the full simulation of the apparatus. Hence, it accounted for the geometry of the instrument, the magnetic field, and all physical processes such as energy losses, multiple scattering, etc. It was found to be constant at 19.9 cm^2 sr above 1 GeV, decreasing smoothly to 8 cm^2 sr at 70 MeV. This decrease was due to the curvature of electrons in the magnetic spectrometer. The *PAMELA* instrumental limit for electrons is $\simeq$47 MeV, below which the particle trajectory hits the magnet walls.

The live time was provided by an on-board clock that timed the periods during which the apparatus was waiting for a trigger. The accuracy of the live time determination was cross-checked by comparing different clocks available in flight, which showed a relative difference of less than 0.2%. The total live time was about 5×10^7 s above $\sim$20 GV, reducing to about 4% of this value at 70 MV because of the relatively short time spent by the satellite at high geomagnetic latitudes.

Because of the wide geomagnetic region spanned by the satellite over its orbit, the electron energy spectrum was evaluated for 16 various vertical geomagnetic cutoff intervals estimated using the satellite position and the Störmer approximation. Figure 11 shows the e^- spectrum measured in five different geomagnetic regions. Two electron components can be clearly seen: the Galactic component at energies higher than the corresponding geomagnetic cutoff and the re-entrant albedo[23] component at lower energies with a transition region where the two components mix. The arrows in Figure 11 indicate the energy region (1.3 times above the maximum vertical geomagnetic cutoff of each interval, i.e., $1.3 \times 0.93 = 1.209$ GeV for the black full circle fluxes and so on) where the fluxes were assumed to be of Galactic origin and unaffected by the Earth's magnetosphere. Then, the final electron spectrum was determined by combining the fluxes of each geomagnetic cutoff interval weighted for its fractional live time.

[23] Particles produced in cosmic-ray interactions with the atmosphere with rigidities lower than the cutoff which, propagating along Earth's magnetic field line, re-enter the atmosphere in the opposite hemisphere but at a similar magnetic latitude.

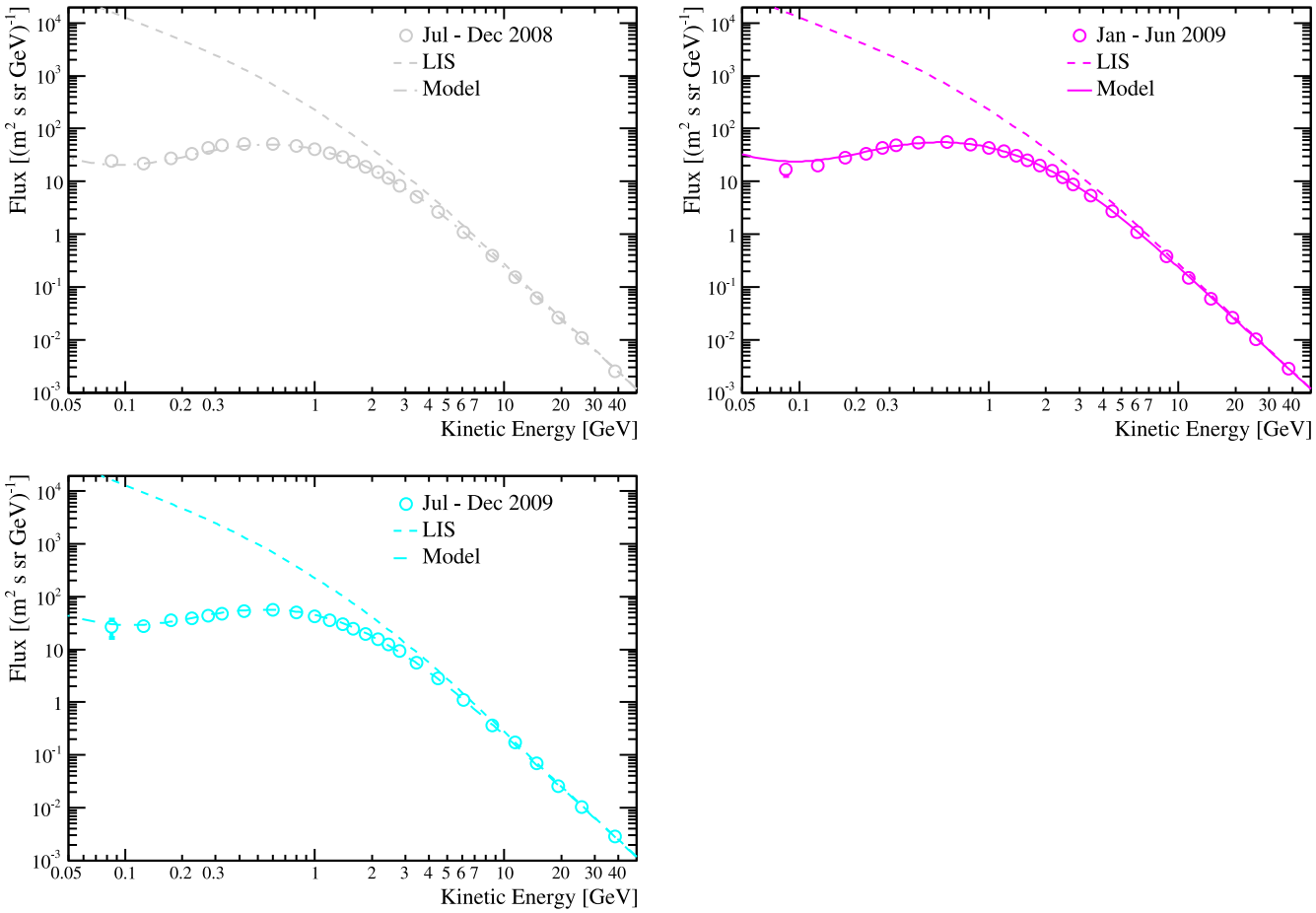

Figure 17. Measured electron (e^-) energy spectrum for the last three half-year periods from the second half of 2008 to the end of 2009. Time progresses from top to bottom and left to right. The error bars are the quadratic sum of the statistical and systematic errors. If not visible, they lie inside the data points. The computed spectra (solid lines) and the LIS used for the computation (dashed line) are also shown.

Possible time-dependent variations of the electron fluxes due to, e.g., not fully estimated time variations of the tracking selection efficiencies, were studied as in the proton analysis (Adriani et al. 2013a). The high-energy (30–50 GeV) proton flux was measured for each half year and with the same selections as in this analysis but the calorimeter selection. The tracking selection efficiencies were estimated with the same Monte Carlo code used for this analysis. Then, the resulting fluxes measured in 2006 July–November were divided by the proton fluxes measured in the other time intervals. Figure 12 shows this ratio as a function of time for fluxes obtained with Criterion 2bis (a) and with Criterion 2 (b). As can be seen, the high-energy proton flux varies a maximum of 2% over the years with the exception of the end of 2009 when the flux estimated with Criterion 2 differs by about 4%. These ratios were used to normalize the electron fluxes measured using both Criteria 2 and 2 bis in each half-year time interval.

In conclusion, the final energy spectra were obtained by correcting the fluxes with these normalization factors and using, as explained in Section 3.1 (see also Section 3.5), Criterion 2bis up to 500 MeV and the significantly more efficient Criterion 2 at higher energies.

3.5. Systematic Uncertainties

Selection efficiencies were obtained by flight and simulated data using efficiency samples. The statistical errors resulting from the finite sizes of such samples were included in the uncertainties of the flux measurements and treated as systematic uncertainties. In the case of efficiencies that deviated from the fitted values beyond statistical fluctuations (e.g., see Figure 8), the deviations were observed to follow a Gaussian distribution and the rms of such a distribution was treated as one standard deviation systematic error (D'Agostini & Raso 2000).

The fluxes were normalized using factors obtained comparing the high-energy proton flux over time. The errors on these factors amounted to less than 1% and were treated as systematic uncertainties. This normalization accounted for the stability of the fluxes estimated for the following time periods, with respect to the second half of 2006. A possible systematic uncertainty on the high-energy proton flux obtained for 2006 July–November and due to the tracking selection efficiency was studied as in Adriani et al. (2011c). An efficiency sample was obtained both from flight and simulated data selecting non-interacting minimum ionizing particles traversing the calorimeter. This required selected protons with rigidities $\sim$2 GV and larger. The resulting simulated and experimental tracking selection efficiency differed by 1.7% and 2.3% when using Criteria 2 and 2bis, respectively. Considering that this experimental efficiency sample was not fully representative of the experimental condition for this analysis, this difference was treated as one standard deviation systematic error.

Table 1
Electron Flux Measured by *PAMELA* between 2006 July and 2008 June

Kinetic Energy (GeV)	Flux (particles/(m^2 sr s GeV))			
	2006 Jul–2006 Nov	2007 Jan–2007 Jun	2007 Jul–2007 Dec	2008 Jan–2008 Jun
0.07–0.10	(7.48 ± 1.32 ± 0.35)	(8.83 ± 1.27 ± 0.41)	(12.48 ± 1.78 ± 0.59)	(20.43 ± 3.03 ± 1.03)
0.10–0.15	(9.60 ± 0.77 ± 0.44)	(11.64 ± 0.74 ± 0.52)	(12.61 ± 0.93 ± 0.57)	(17.52 ± 1.41 ± 0.81)
0.15–0.20	(13.95 ± 0.75 ± 0.64)	(15.69 ± 0.70 ± 0.70)	(19.18 ± 0.92 ± 0.86)	(22.25 ± 1.21 ± 1.01)
0.20–0.25	(18.74 ± 1.03 ± 0.86)	(21.11 ± 0.95 ± 0.95)	(27.99 ± 1.32 ± 1.26)	(29.07 ± 1.65 ± 1.32)
0.25–0.30	(23.68 ± 1.04 ± 1.11)	(25.99 ± 0.95 ± 1.17)	(34.07 ± 1.31 ± 1.54)	(35.03 ± 1.60 ± 1.62)
0.30–0.35	(26.10 ± 1.05 ± 1.22)	(31.15 ± 1.00 ± 1.40)	(38.92 ± 1.34 ± 1.75)	(38.78 ± 1.61 ± 1.77)
0.35–0.50	(32.56 ± 0.71 ± 1.50)	(36.23 ± 0.65 ± 1.62)	(41.44 ± 0.82 ± 1.85)	(43.01 ± 1.01 ± 1.93)
0.50–0.70	(35.51 ± 0.59 ± 1.73)	(39.85 ± 0.51 ± 1.88)	(44.71 ± 0.61 ± 2.10)	(46.44 ± 0.70 ± 2.20)
0.70–0.90	(34.26 ± 0.42 ± 1.66)	(39.71 ± 0.38 ± 1.87)	(43.48 ± 0.44 ± 2.04)	(43.90 ± 0.50 ± 2.08)
0.90–1.10	(31.26 ± 0.40 ± 1.52)	(34.90 ± 0.35 ± 1.64)	(37.25 ± 0.40 ± 1.75)	(37.37 ± 0.45 ± 1.77)
1.10–1.30	(27.93 ± 0.38 ± 1.36)	(30.03 ± 0.32 ± 1.42)	(31.43 ± 0.36 ± 1.48)	(32.52 ± 0.42 ± 1.54)
1.30–1.50	(23.64 ± 0.28 ± 1.15)	(26.01 ± 0.24 ± 1.23)	(26.48 ± 0.27 ± 1.25)	(27.09 ± 0.31 ± 1.29)
1.50–1.70	(20.00 ± 0.26 ± 0.97)	(21.96 ± 0.22 ± 1.04)	(22.47 ± 0.25 ± 1.06)	(22.64 ± 0.28 ± 1.07)
1.70–2.00	(16.59 ± 0.19 ± 0.81)	(17.68 ± 0.16 ± 0.83)	(18.10 ± 0.18 ± 0.85)	(18.15 ± 0.20 ± 0.86)
2.00–2.30	(13.24 ± 0.16 ± 0.64)	(14.21 ± 0.13 ± 0.67)	(14.19 ± 0.15 ± 0.67)	(13.88 ± 0.16 ± 0.65)
2.30–2.60	(10.41 ± 0.12 ± 0.50)	(10.94 ± 0.10 ± 0.51)	(11.31 ± 0.12 ± 0.53)	(10.97 ± 0.13 ± 0.52)
2.60–3.00	(7.77 ± 0.09 ± 0.38)	(8.01 ± 0.08 ± 0.38)	(8.27 ± 0.09 ± 0.39)	(8.19 ± 0.10 ± 0.39)
3.00–4.00	(4.78 ± 0.05 ± 0.23)	(4.88 ± 0.04 ± 0.23)	(5.07 ± 0.05 ± 0.24)	(4.97 ± 0.05 ± 0.23)
4.00–5.00	(2.51 ± 0.03 ± 0.12)	(2.64 ± 0.03 ± 0.12)	(2.60 ± 0.03 ± 0.12)	(2.58 ± 0.03 ± 0.12)
5.00–7.50	(1.05 ± 0.01 ± 0.05)	(1.07 ± 0.01 ± 0.05)	(1.08 ± 0.01 ± 0.05)	(1.05 ± 0.01 ± 0.05)
7.50–10.00	$(3.73 \pm 0.07 \pm 0.18) \times 10^{-1}$	$(3.77 \pm 0.06 \pm 0.18) \times 10^{-1}$	$(3.68 \pm 0.06 \pm 0.17) \times 10^{-1}$	$(3.72 \pm 0.07 \pm 0.18) \times 10^{-1}$
10.00–13.00	$(1.41 \pm 0.03 \pm 0.07) \times 10^{-1}$	$(1.53 \pm 0.03 \pm 0.07) \times 10^{-1}$	$(1.56 \pm 0.03 \pm 0.07) \times 10^{-1}$	$(1.48 \pm 0.04 \pm 0.07) \times 10^{-1}$
13.00–17.00	$(6.15 \pm 0.18 \pm 0.30) \times 10^{-2}$	$(6.37 \pm 0.15 \pm 0.30) \times 10^{-2}$	$(6.20 \pm 0.17 \pm 0.29) \times 10^{-2}$	$(6.24 \pm 0.19 \pm 0.29) \times 10^{-2}$
17.00–22.00	$(2.64 \pm 0.10 \pm 0.13) \times 10^{-2}$	$(2.59 \pm 0.08 \pm 0.12) \times 10^{-2}$	$(2.40 \pm 0.08 \pm 0.11) \times 10^{-2}$	$(2.70 \pm 0.10 \pm 0.13) \times 10^{-2}$
22.00–30.00	$(1.08 \pm 0.05 \pm 0.05) \times 10^{-2}$	$(1.11 \pm 0.04 \pm 0.05) \times 10^{-2}$	$(1.12 \pm 0.05 \pm 0.05) \times 10^{-2}$	$(1.03 \pm 0.05 \pm 0.05) \times 10^{-2}$
30.00–50.00	$(2.97 \pm 0.16 \pm 0.14) \times 10^{-3}$	$(2.60 \pm 0.12 \pm 0.12) \times 10^{-3}$	$(2.77 \pm 0.14 \pm 0.13) \times 10^{-3}$	$(2.51 \pm 0.15 \pm 0.12) \times 10^{-3}$

Note. The first and second errors represent the one standard deviation statistical and systematic errors, respectively.

As a check of the consistency of the evaluation of the selection efficiencies the energy spectrum of each time interval obtained with Criterion 2 was compared with the equivalent one obtained with Criterion 2bis. Figure 13 shows the ratios of the two sets of fluxes for each time interval. The solid lines indicate the systematic uncertainties associated with the efficiencies. Above 500 MeV, the two sets of fluxes agree perfectly within the systematic uncertainties showing that systematic errors were properly assigned to the selection efficiencies. Below 500 MeV, the fluxes obtained with Criterion 2 are consistently higher because of the contamination by spillover protons caused by the less stringent selection, as discussed in Section 3.1.

An additional check was performed to validate the estimation of the low energy (<1 GeV) fluxes. The low-energy part of the re-entrant albedo e^- spectrum was measured at the lowest geomagnetic latitude (vertical geomagnetic cutoff greater than 12.1 GV) in each time interval and it was compared to the same spectrum measured in the second half of 2006. It has been shown (Lipari 2002; Zuccon et al. 2003) that, because of the east–west effect, re-entrant albedos e^- at low geomagnetic latitudes, i.e., high geomagnetic cutoffs, are mostly produced by high-energy (⩾30 GeV) protons interacting with the Earth's atmosphere. Therefore, it can be inferred that the re-entrant albedo e^- energy spectrum should not show significant temporal variations due to solar modulation, and hence it can be used to check the temporal stability of the flux measurements at the lowest energies. Figure 14 shows the re-entrant albedo e^- fluxes measured in 2006 July–November divided by the equivalent fluxes measured in the other time intervals. The solid lines indicate the systematic uncertainties associated with these data. No significant time variation was found, indicating that the systematic uncertainties properly accounted for any residual time dependence down to the lowest measured energies.

The unfolding procedure was a significant correction for the electron spectra, therefore the corresponding uncertainties were carefully studied. It was shown in the proton analysis (Adriani et al. 2011c) that this procedure was able to account for the intrinsic spatial resolution and the alignment uncertainty of the spectrometer silicon sensors. The related uncertainties, as well as the additional effects due to the significant energy losses and reduced statistical significance of the count distribution, were studied by folding and unfolding a known spectral shape. A large sample of electrons was simulated with an input spectrum consistent with the reconstructed experimental spectrum at the top of the payload for the lowest geomagnetic cutoff rigidity interval. Then the rigidities of the simulated events were reconstructed and 100 different count distributions were built as in the analysis. The statistics of each count distribution were comparable to the experimental statistics for a geomagnetic cutoff interval. Then the count distributions were unfolded and compared with the large simulated sample by means of pull distributions (Eadie et al. 1971). These pull distributions followed the expected standard normal distribution with sigma consistent with one, hence the statistical errors properly accounted for the fluctuations in the flux values and means that fluctuated around zero. The relative differences between

Table 2
Electron Flux Measured by *PAMELA* between 2008 July and 2009 December

Kinetic Energy (GeV)	Flux (particles/(m^2 sr s GeV))		
	2008 Jul–2008 Dec	2009 Jan–2009 Jun	2009 Jul–2009 Dec
0.07–0.10	(24.19 ± 4.82 ± 1.31)	(16.89 ± 3.99 ± 0.92)	(26.68 ± 9.65 ± 1.95)
0.10–0.15	(21.79 ± 2.28 ± 1.04)	(19.91 ± 2.27 ± 0.96)	(27.52 ± 4.57 ± 1.57)
0.15–0.20	(27.45 ± 1.94 ± 1.27)	(28.40 ± 2.14 ± 1.33)	(35.09 ± 3.95 ± 1.89)
0.20–0.25	(32.92 ± 2.45 ± 1.51)	(33.29 ± 2.61 ± 1.54)	(38.23 ± 4.37 ± 2.01)
0.25–0.30	(43.45 ± 2.55 ± 2.02)	(42.50 ± 2.64 ± 2.02)	(42.79 ± 4.01 ± 2.29)
0.30–0.35	(47.75 ± 2.54 ± 2.20)	(48.34 ± 2.70 ± 2.28)	(47.83 ± 3.97 ± 2.52)
0.35–0.50	(51.70 ± 1.55 ± 2.33)	(54.00 ± 1.70 ± 2.46)	(52.67 ± 2.52 ± 2.66)
0.50–0.70	(50.87 ± 0.95 ± 2.42)	(54.92 ± 1.03 ± 2.64)	(56.79 ± 1.54 ± 3.03)
0.70–0.90	(46.72 ± 0.68 ± 2.22)	(49.95 ± 0.72 ± 2.40)	(50.35 ± 1.05 ± 2.67)
0.90–1.10	(40.51 ± 0.62 ± 1.93)	(42.88 ± 0.66 ± 2.06)	(42.72 ± 0.95 ± 2.27)
1.10–1.30	(34.41 ± 0.56 ± 1.64)	(36.86 ± 0.61 ± 1.77)	(35.85 ± 0.87 ± 1.91)
1.30–1.50	(28.92 ± 0.42 ± 1.38)	(30.39 ± 0.45 ± 1.47)	(29.94 ± 0.65 ± 1.60)
1.50–1.70	(23.62 ± 0.37 ± 1.13)	(25.17 ± 0.40 ± 1.21)	(24.38 ± 0.57 ± 1.30)
1.70–2.00	(18.92 ± 0.27 ± 0.90)	(20.15 ± 0.29 ± 0.97)	(19.71 ± 0.41 ± 1.05)
2.00–2.30	(14.97 ± 0.22 ± 0.71)	(15.72 ± 0.24 ± 0.75)	(15.58 ± 0.34 ± 0.82)
2.30–2.60	(11.57 ± 0.17 ± 0.55)	(12.05 ± 0.19 ± 0.57)	(12.37 ± 0.28 ± 0.65)
2.60–3.00	(8.36 ± 0.13 ± 0.40)	(8.75 ± 0.14 ± 0.42)	(9.23 ± 0.21 ± 0.49)
3.00–4.00	(5.12 ± 0.07 ± 0.24)	(5.31 ± 0.07 ± 0.25)	(5.55 ± 0.11 ± 0.29)
4.00–5.00	(2.63 ± 0.04 ± 0.12)	(2.73 ± 0.05 ± 0.13)	(2.85 ± 0.07 ± 0.15)
5.00–7.50	(1.08 ± 0.02 ± 0.05)	(1.10 ± 0.02 ± 0.05)	(1.09 ± 0.03 ± 0.06)
7.50–10.00	(3.88 ± 0.09 ± 0.18) × 10^{-1}	(3.84 ± 0.10 ± 0.18) × 10^{-1}	(3.67 ± 0.14 ± 0.19) × 10^{-1}
10.00–13.00	(1.53 ± 0.05 ± 0.07) × 10^{-1}	(1.47 ± 0.05 ± 0.07) × 10^{-1}	(1.71 ± 0.08 ± 0.09) × 10^{-1}
13.00–17.00	(6.08 ± 0.24 ± 0.29) × 10^{-2}	(6.06 ± 0.25 ± 0.29) × 10^{-2}	(6.87 ± 0.40 ± 0.36) × 10^{-2}
17.00–22.00	(2.61 ± 0.13 ± 0.12) × 10^{-2}	(2.65 ± 0.14 ± 0.13) × 10^{-2}	(2.53 ± 0.20 ± 0.13) × 10^{-2}
22.00–30.00	(1.08 ± 0.06 ± 0.05) × 10^{-2}	(1.01 ± 0.06 ± 0.05) × 10^{-2}	(1.03 ± 0.10 ± 0.06) × 10^{-2}
30.00–50.00	(2.57 ± 0.20 ± 0.01) × 10^{-3}	(2.82 ± 0.22 ± 0.14) × 10^{-3}	(2.84 ± 0.32 ± 0.16) × 10^{-3}

Note. The first and second errors represent the one standard deviation statistical and systematic errors, respectively.

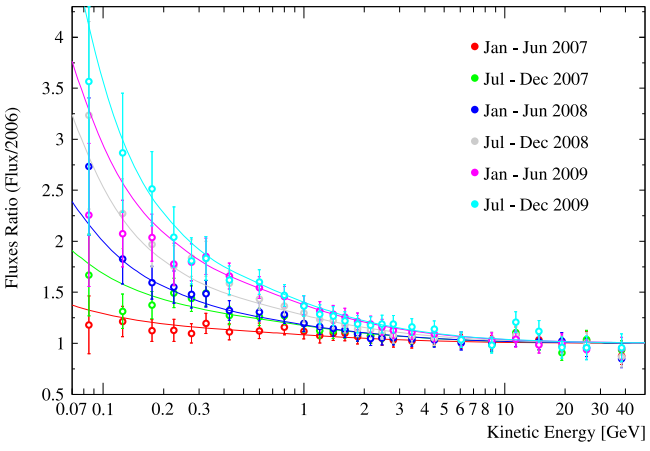

Figure 18. Ratios as a function of energy between the measured half-year (e^-) fluxes from 2007 January to 2009 December and the measured fluxes for the period 2006 July–November overlaid with the corresponding computed spectra (solid lines). The error bars are the quadratic sums of the statistical and systematic errors.

the means of the expected and reconstructed count distributions could be approximated with a Gaussian distribution. Following D'Agostini & Raso (2000), the rms of this distribution, amounting to 4%, was treated as one standard deviation systematic error due to the unfolding procedure.

The unfolding procedure was also tested comparing the resulting electron energy spectrum with the one obtained estimating the electron energy from the total energy deposited in the calorimeter (for more information see Adriani et al. 2014). A difference of 2% at 2 GeV increasing to 6% at 10 GeV and then decreasing to less than 1% above 30 GeV was found between the two approaches. This difference is consistent with the previously estimated unfolding uncertainty. Hence, even if it may also account for additional uncertainties such as those on thickness and density of the materials above the tracking system, it was not added to the uncertainty of the unfolding procedure.

Finally, the full analysis chain was cross-checked with simulations. Electron events were simulated at the top of the payload with isotropic arrival directions and with an energy spectrum from 40 MeV to 100 GeV consistent with the reconstructed experimental spectrum for the first geomagnetic cutoff interval (0–0.055 GV). Then the events that, according to simulation, triggered the instrument were processed with the *PAMELA* data analysis software and consequently treated as in the experimental analysis (rigidity determination, selection based on Criteria 1–8, efficiency and unfolding corrections, flux determination). The resulting energy spectrum was compared with the input one and a good agreement was found. The differences between the input and reconstructed fluxes at the top of the payload were consistent with the uncertainties related to the unfolding procedure described in the previous paragraphs. Therefore, it was concluded that the analysis procedure did not introduce additional uncertainties.

Figure 15 shows the relative errors resulting from the quadratic sum of the systematic uncertainties discussed here.

Evidently, the uncertainty is higher at low rigidities where the Criterion 2bis is used, and it increases over time, essentially because of the decreasing efficiency of the tracking system.

4. RESULTS

Figures 16 and 17 and Tables 1 and 2 show the resulting electron (e^-) energy spectra for the seven half-year periods. The error bars are the quadratic sum of the statistical and systematic errors. The electron spectra for each time interval are overlaid with the corresponding computed spectra (solid lines) with respect to the LIS (dashed lines), which is based on *Voyager 1* observations (Stone et al. 2013) at low energies. This LIS was described by Potgieter et al. (2013b); see also the review by Potgieter (2014a). The full three-dimensional numerical model was described in detail by Potgieter et al. (2014). It is based on the numerical solution of Parker's transport equation (Parker 1965), including all four major modulation mechanisms: convection, diffusion described by a full 3D tensor, particle drifts caused by gradients, curvatures and the current sheet in the HMF, and adiabatic energy changes.

Averaging these fluxes over the whole time period (2006 July–2009 December), the resulting absolute energy spectrum was compared to the previously published results (Adriani et al. 2011b). This new estimation yields fluxes whose absolute values are approximately 10% higher than in the previous work. This difference stems from an improved treatment both in the data and in the simulation of the time dependence of the tracking system performances and unfolding procedure.

Figure 18 shows the ratios as a function of energy between the measured half-year period fluxes from 2007 January until 2009 December and the fluxes measured in the first period of data taking (2006 July–November). It follows from these ratios that the low-energy electron flux increased by a factor of about 1.6 from 2006 to 2009 at about 0.5 GeV. Protons at corresponding rigidities, on the other hand, increased by a factor of about 2.4 over this period (Adriani et al. 2013a; Potgieter et al. 2014), indicating the effect of particle drifts. Furthermore, the comparison between the model simulations and observations shows that the electron spectrum became progressively softer, more than expected from drift model predictions. This requires larger diffusion coefficients at lower energies (kinetic energy $<$200 MeV) than anticipated. Details concerning the electron modulation model with theoretical assumptions and implications will be published in an accompanying paper (Potgieter et al. 2015).

5. CONCLUSIONS

We have presented new results on the electron (e^-) energy spectrum between 70 MeV and 50 GeV obtained by the *PAMELA* experiment during the past extraordinary solar minimum period that ended in late 2009–beginning of 2010. By comparing the observations with the model as described in an accompanying paper (Potgieter et al. 2015) valuable insight is gained into what caused electron modulation over this unusual solar minimum period.

We acknowledge support from the Italian Space Agency (ASI), Deutsches Zentrum für Luft- und Raumfahrt (DLR), the Swedish National Space Board, the Swedish Research Council, the Russian Space Agency (Roscosmos), and the Russian Science Foundation. M. Potgieter and E. Vos acknowledge partial financial support from the South African Research Foundation (NRF) under the SA–Italy Bilateral Programme.

REFERENCES

Ackermann, M., Ajello, M., Allafort, A., et al. 2012, PhRvL, 108, 011103
Adriani, O., Barbarino, G. C., Bazilevskaya, G. A., et al. 2009a, Natur, 458, 607
Adriani, O., Barbarino, G. C., Bazilevskaya, G. A., et al. 2009b, PhRvL, 102, 051101
Adriani, O., Barbarino, G. C., Bazilevskaya, G. A., et al. 2010, APh, 34, 1
Adriani, O., Barbarino, G. C., Bazilevskaya, G. A., et al. 2011a, ApJ, 742, 102
Adriani, O., Barbarino, G. C., Bazilevskaya, G. A., et al. 2011b, PhRvL, 106, 201101
Adriani, O., Barbarino, G. C., Bazilevskaya, G. A., et al. 2013a, ApJ, 765, 91
Adriani, O., Barbarino, G. C., Bazilevskaya, G. A., et al. 2013b, PhRvL, 111, 081102
Adriani, O., Barbarino, G. C., Bazilevskaya, G. A., et al. 2014, PhR, 544, 323
Adriani, O., Bonechi, L., Bongi, M., et al. 2003, NIMPA, 511, 72
Adriani, O., Barbarino, G. C., Bazilevskaya, G. A., et al. 2011c, Sci, 332, 69
Agostinelli, S., Allison, J., Amako, K., et al. 2003, NIMPA, 506, 250
Aguilar, M., Alberti, G., Alpat, B., et al. 2013, PhRvL, 110, 141102
Aharonian, F., Akhperjanian, A. G., Aye, K.-M., et al. 2004, Natur, 432, 75
Allen, G. E., Keohane, J. W., Gotthelf, E. V., et al. 1997, ApJL, 487, L97
Atoyan, A. M., Aharonian, F. A., & Völk, H. J. 1995, PhRvD, 52, 3265
Bisschoff, D., & Potgieter, M. S. 2014, ApJ, 794, 166
Boezio, M., Bonvicini, V., Mocchiutti, E., et al. 2002, NIMPA, 487, 407
Cirelli, M., Kadastik, M., Raidal, M., & Strumia, A. 2008, NuPhB, 813, 1
D'Agostini, G. 1995, NIMPA, 362, 487
D'Agostini, G., & Raso, M. 2000, arXiv:hep-ex/0002056
Delahaye, T., Lavalle, J., Lineros, R., Donato, F., & Fornengo, N. 2010, A&A, 524, A51
Eadie, W. T., Drijard, D., James, F. E., et al. 1971, Statistical Methods in Experimental Physics (Amsterdam: North Holland Publishing), 1
Gurnett, D. A., Kurth, W. S., Burlaga, L. F., & Ness, N. F. 2013, Sci, 341, 1489
Lipari, P. 2002, APh, 16, 295
Mewaldt, R. A. 2010, ApJL, 723, 1
Munini, R. 2012, Master thesis, Univ. Trieste
Orsi, S., Carlson, P., Hofverberg, P., Lund, J., & Pearce, M. 2005, in Proc. ICRC, 3, 369
Osteria, G., Campana, D., Barbarino, G., et al. 2004, NIMPA, 535, 152
Parker, E. N. 1965, P&SS, 13, 9
Picozza, P., Galper, A. M., Castellini, G., et al. 2007, APh, 27, 296
Potgieter, M. S. 2013, LRSP, 10, 3
Potgieter, M. S. 2014a, BrJPh, 44, 581
Potgieter, M. S. 2014b, AdSpR, 53, 1415
Potgieter, M. S., Strauss, R., Du, T., DeSimone, N., & Boezio, M. 2013a, Proc. ICRC (Rio de Janeiro, Brazil), arXiv:1308.1617
Potgieter, M. S., Vos, E. E., Boezio, M., Di Felice, V., & Munini, R. 2015, ApJ, 810, 141
Potgieter, M. S., Vos, E. E., Boezio, M., et al. 2014, SoPh, 289, 391
Potgieter, M. S., Vos, E. E., Nndanganeni, R. R., Boezio, M., & Munini, R. 2013b, Proc. ICRC (Rio de Janeiro. Brazil), arXiv:1308.1666
Stone, E. C., Cummings, A. C., McDonald, F. B., et al. 2013, Sci, 341, 150
Stozhkov, Y. I., Basili, A., Bencardino, R., et al. 2005, IJMPA, 20, 6745
Strauss, R. D., & Potgieter, M. S. 2014a, AdSpR, 53, 1015
Strauss, R. D., & Potgieter, M. S. 2014b, SoPh, 289, 3197
Webber, W. R., Higbie, P. R., & McDonald, F. B. 2013, arXiv:1308.4426
Zuccon, P., Bertucci, B., Alpat, B., et al. 2003, APh, 20, 221